Carbon 161 (2020) 71–82

Contents lists available at ScienceDirect

Carbon

journal homepage: www.elsevier.com/locate/carbon

Tuning the electronic, mechanical, thermal, and optical properties of tetrahexcarbon via hydrogenation

Mehmet Emin Kilic *, Kwang-Ryeol Lee **

Computational Science Research Center, Korea Institute of Science and Technology, Seoul, 02792, Republic of Korea

ARTICLE INFO

Article history:
Received 13 November 2019
Received in revised form
31 December 2019
Accepted 7 January 2020
Available online 18 January 2020

ABSTRACT

Recently, Tetrahexcarbon (TH-carbon), a new two-dimensional(2D) carbon allotrope, has been identified with an intrinsic direct bandgap, which makes it promising for practical applications in optoelectronic devices. Using first-principles calculations, we examined the possibility of manipulating the physical and chemical properties of TH-carbon sheet by controlled hydrogenation. We systematically studied pristine TH-carbon and its hydrogenated derivatives with various configurations such as single- and double-sided hydrogenation. Our study revealed their stability in energetic, dynamic, thermal, and mechanical aspects. Depending on the hydrogen coverage and configurations, we observed the tunability of the phononic and electronic bandgap, and the direct-indirect-direct bandgap transitions. These results suggest the plausibility of modulating its electronic properties by hydrogenation. The heat transport in TH-carbon is anisotropic. A significant decrease in thermal conductivity was observed in the fully hydrogenated TH-carbon. The thermal conductivity in TH-carbon can be controlled by the sp^3 C–H low conduction domains. A notable increase in specific heat capacity was observed in hydrogenated derivatives of TH-carbon, which would make them useful in nanoscale engineering of thermal transport. The hydrogenation was found to reduce the in-plane stiffness and Young's modulus, but increase the ultimate strength. These findings would provide important guidelines for practical applications of TH-carbon.

1. Introduction

The growing list of available two dimensional (2D) crystals consists of graphene [1] and the graphene derivatives (graphane [2,3] and graphene fluoride [4]), graphyne [5], silicene [6], hexagonal boron nitride [7], MoS_2, and many more [8–12]. Graphene, as the most stable 2D form of carbon, has received a great deal of attention from experimentalists and theoreticians due to its superior properties such as the robustness, stability, flexibility, zero-gap, Dirac cone electronic structure, and high electron mobility [1,13–15]. Motivated by the discovery of graphene, great efforts have been made on the discovery of new carbon allotrope beyond graphene. Carbon possesses different hybridization states such as sp, sp^2, and sp^3 ones, leads to the formation of new carbon allotrope with quite different chemical and physical properties. For instance, sp^2-hybridized graphene is a soft and zero band gap semiconductor whereas sp^3-hybridized diamond has excellent hardness and insulating property [1,16].

By combining the different hybridization states, numerous 2D carbon allotropes such as graphyne family ($sp - sp^2$) [17–21], penta-graphene (PG) ($sp^2 - sp^3$) [22], and Tetrahexcarbon (TH-carbon) ($sp^2 - sp^3$) [23] have been predicted. Their novel properties such as Dirac cone [24], good thermal conductivity, and extreme hardness have been extensively examined. For instance, graphyne and its family have graphene-like electronic properties (Dirac cone), and 6,6,12-graphyne has more amazing electronic and transport properties than that of graphene [25]. Grazynes, based on graphene stripes linked to each other by acetylenic connections, are reported to be stiffer than graphene [26]. PG exclusively composed of carbon pentagons [22], exhibits an unusual negative Poisson's ratio and ultrahigh ideal strength [27], which would make PG useful for many practical applications. In 2018, by applying Stone-Wales transformation in PG, TH-carbon has been predicted to be energetically favorable than PG [23]. TH-carbon exhibits remarkable properties such as a wide direct band gap, highly anisotropic electronic properties, and high electron mobility, which make it promising for nanoelectronics and optoelectronic devices [23,28].

Designing the hybridization states of the carbon allotrope would be useful to control its physical and chemical properties. Chemical

* Corresponding author.
** Corresponding author.
E-mail addresses: mekilic@kist.re.kr (M.E. Kilic), krlee@kist.re.kr (K.-R. Lee).

https://doi.org/10.1016/j.carbon.2020.01.027
0008-6223/

functionalization (including H, F, O, OH, etc.) is an effective way to transform the hybridization state of carbons. For instance, sp^3-hybridized graphene (namely graphane [2,3]) is obtained by completely hydrogenated configurations of sp^2-hybridized graphene. The surface functionalization by hydrogen for 2D carbon allotropes has received much attention to enhance their intrinsic properties [3,29–37]. Hydrogenation of graphene turns the semimetallic feature into a wide band gap semiconductor, induces magnetic moments, and dramatically changes its transport properties [2,38–42]. Furthermore, hydrogenated PG indicates a notable enhancement in thermal conductivity [43]. Therefore, hydrogenation is an effective way to tune the electronic, magnetic, and thermal properties of 2D carbon allotropes. So far, the role of hydrogen atoms by surface modification of the TH-carbon has yet to be reported.

Herein, we systematically studied the pristine TH-carbon and its hydrogenated derivatives with various configurations such as single- and double-sided hydrogenation within the framework of density functional theory (DFT). Firstly, we tested the stability of the hydrogenated TH-carbon structures. We verified their stabilities from energetic, dynamic, thermal, and mechanical aspects by the computation results of binding energy, phonon band structure, thermal stability, and elastic constants. After confirming their stabilities, we examined their structural, mechanical, thermal, electronic, and optical properties. Our results showed that depending on the hydrogen coverage and configurations, its phononic and electronic band gap can be tuned and the direct-indirect-direct band gap transitions can be obtained. The thermal transport in TH-carbon was found to be anisotropic. A significant decrease in thermal conductivity was observed by hydrogenation. The heat transport in TH-carbon can be controlled by the sp^3 C–H low conduction domains. Moreover, a notable increase in specific heat capacity was observed in hydrogenated derivatives of TH-carbon. Furthermore, the hydrogenation is found to reduce the in-plane stiffness and Young's modulus but increase the ultimate strength. The anisotropic optical behavior in TH-carbon due to the inherent structural anisotropy turn to isotropic by hydrogenation.

2. Methodology

First-principles calculations and *ab-initio* molecular dynamics (AIMD) calculations were performed within framework of density functional theory (DFT) formalism as implemented in the VASP software package [44]. The well-established projector augmented wave method (PAW) [45,46] was applied with an energy cutoff of 520 eV for the plane wave basis. Gaussian smearing with a width of $\sigma = 0.01$ eV was used in the calculations. For the exchange correlation energy functional, the generalized gradient approximation (GGA) was employed in the Perdew – Burke – Ernzerhof (PBE) scheme [47]. The first Brillouin zone (BZ) integration was performed using Monkhorst-Pack scheme [48]. We utilized $24 \times 24 \times 1$ and $12 \times 12 \times 1$ k-point mesh for the $1 \times 1 \times 1$ and $2 \times 2 \times 1$ TH-carbon systems respectively, which were accurate enough based on our test calculations. To ensure isolation and reduce the artificial interactions between periodic images in the perpendicular direction, a vacuum region of 20 Å was included in the cubic large simulation cell. In the energy minimization using the conjugate gradient method, we allowed all atoms in the sheet to fully relax without any constraint. In all these calculations, the convergence criteria for total energy in self-consistent field iteration was set to 1×10^{-5} eV. The structures were optimized by keeping the volume of the unit cell constant until the Hellmann – Feynman force component on each atom was less than 0.001 eV Å^{-1}. After the full structural optimization with the PBE functional, we evaluated the accurate band gap energy from the Heyd-Scuseria-Ernzerhof (HSE) hybrid functional, constructed by mixing 25% of nonlocal Fock exchange with 75% of PBE exchange and 100% of PBE correlation energy [49,50].

To calculate the binding energy (E_b) of the hydrogen atom(s) on TH-carbon as a function of x, where x was the concentration of H in CH_x, it was used the following expression:

$$E_b = \left(E_{TH-carbon} + nE_H - E^x_{TH-carbon/nH}\right) \Big/ n \quad , \tag{1}$$

where $E_{TH-carbon}$, E_H, and $E^x_{TH-carbon/nH}$ are the total energies of pristine TH-carbon, an isolated hydrogen atom(s), and the hydrogenated TH-carbon with a x concentration of H and n was the number of attached H atoms per unit cell for given x. $E_b > 0$ implies the adsorption was energetically favorable.

In AIMD simulations, the convergence criterion of total energy was set as 1×10^{-4} eV. The calculations were performed in $4 \times 4 \times 1$ supercell, with the temperature starting from 300 K and then gradually being increased up to 900 K. Temperature control was achieved using Nose-Hover thermostat [51–53]. The time step used for the integration of equations of motion was set to $t = 1$ fs, and the total time for the simulation was 2.5 ps.

To reveal the dynamics stability of the system, the phonon spectrum was calculated using finite displacement method implemented in Phonopy code [54]. The second-order interatomic force constants (IFC) can be attained by using a $4 \times 4 \times 1$ supercell with $3 \times 3 \times 1$ $k-$ mesh, and very high accuracy (the convergence criterion of total energy was set as 1×10^{-8} eV) for the phonon dispersion calculations of TH-carbon systems. The third-order IFCs can attained by $2 \times 2 \times 1$ supercell with $2 \times 2 \times 1$ $k-$ mesh by Pho-no3py package [55].

To examine the diffusion barrier of the single hydrogen atom on TH-carbon, the climbing-image NEB method [56] was used to find minimum energy paths (MEP) and transition states (TS) from given the initial state (IS) and final state (FS). The IS and FS were taken the same cell shape and volume. An interpolated chain of configurations (images) between IS and FS positions were connected by springs and relaxed simultaneously. The seven linearly interpolated images between two energetic sites (IS and FS) for single H atom diffusion were taken. All the images were relaxed until the maximum force acting on atom was less than 0.01 eV Å^{-1}. All saddle points were then verified to be true TS.

To examine the chemical bonding environment for sp^2 and sp^3-hybridized carbon atoms, the electron localization function (ELF) as an ideal visualization tool [57] is calculated using the Kohn-Sham DFT orbitals.

3. Results and discussion

3.1. Pristine tetrahexcarbon

The unitcell of the pristine TH-carbon as shown in Fig. 1 (a) was used as a basic model to investigate the properties of hydrogenated systems. Before investigating the hydrogenated systems, we first performed the structural optimization of pristine TH-carbon where carbon atoms are arranged in three atomic planes: the lower and the upper planes are formed by sp^2-hybridized carbon atoms (denoted as C_1), and the middle plane contains sp^3-hybridized carbon atoms (denoted as C_2). Contrary to graphene (all the carbon atoms are equivalent to sp^2-hybridization), TH-carbon thus consists of two chemically inequivalent carbon atoms (C_1 and C_2). After structural optimization, the fully relaxed lattice constants of the TH-carbon within the rectangular unit cell are found to be $a = 4.53$ Å and $b = 6.11$ Å. The calculated bond lengths between two C_1 atoms and between C_1 and C_2 atoms are $d_{11} = 1.34$ Å and $d_{12} =$

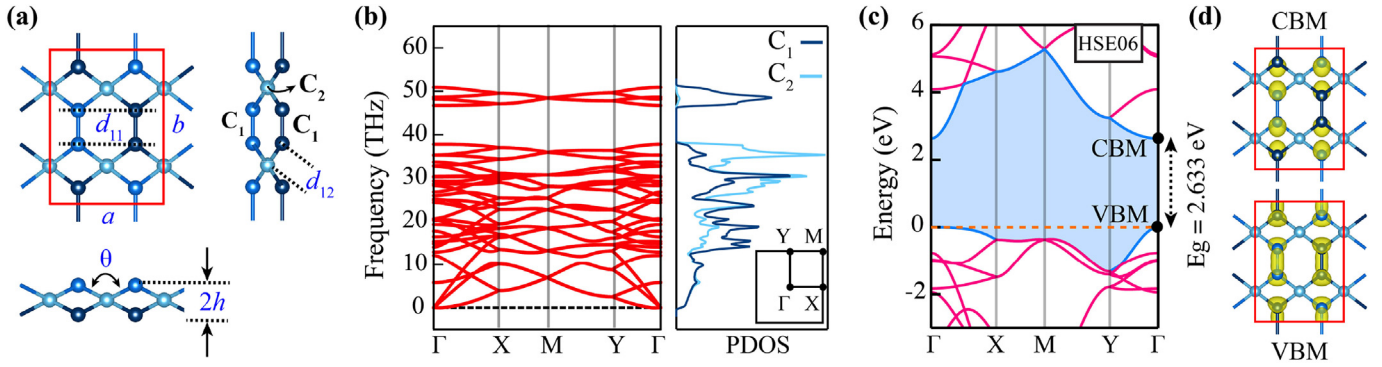

Fig. 1. (a) Structure of pristine TH-carbon, containing eight sp^2- and four sp^3-hybridized carbon atoms (labeled as C_1 and C_2, respectively) in unit cell (framed by the red line). The C_1 atoms are forming two external layers $z = \pm h$ while the C_2 atoms lie on the middle layer with $z = 0$. Here, the top view from the z direction (upper panel left), side view from the x direction (upper panel right), and the side view from the y direction (lower panel) of TH-carbon are separately shown. Lattice constants (a and b), the buckling height (h), bond lengths (d_{11} and d_{12}) are depicted. All the blue spheres in the lattice refer to the carbon atoms. (b) Phonon dispersion curve along with the high symmetric k points given by the 2D-rectangular Brillouin zone (inset) and atom projected phonon density of state (PDOS). (c) Electronic band structure obtained from HSE06 method. Note that the Fermi level energy (E_F) is set to zero (depicted by the orange dashed line). (d) Charge density of conduction band minimum (CBM) and valence band maximum (VBM) is given in upper and lower panels, respectively. Here, iso-surface of the charge density (yellow color lobes) is 0.0015 e/Å^3. (A colour version of this figure can be viewed online.)

1.54 Å, respectively. The pristine TH-carbon has a buckled structure with buckling height of $h = 0.58$ Å, and the angle between carbon atoms (C_1–C_2–C_1 bond angle) is found to be $\theta = 135.51^\circ$. These structural parameters are in good agreement with the report of Ram et al. [23]. The calculated phonon band structure, electronic band structure, and charge density of TH-carbon are respectively given in Fig. 1 (b), (c), and (d) which will be discussed in the following sections.

3.2. Hydrogenated tetrahexcarbon

We examined the hydrogenated derivatives of TH-carbon by considering the single- and double-sided adsorption of hydrogen. We tested their stability in energetic, dynamic, thermal, and mechanical aspects. After that, their structural, mechanical, thermal, electronic, and optical properties were investigated. The results of the structural properties of TH-carbon and its hydrogenated derivatives are summarized in Table 1.

3.2.1. Atomic structure and structural characteristics

We first studied the interaction of a single hydrogen atom with the TH-carbon (denoted as H/TH-carbon) using spin-polarized DFT calculations. To determine the most energetically favorable binding site for H/TH-carbon, we considered nine different possible adsorption sites in the 2×2 supercell as presented in Fig. 2 (a). Our results indicate that the single hydrogen atom can be chemically bonded to the top of C_1 atom (denoted as T_1 site) with the binding energy of 2.45 eV. The C_1 atom just underneath the hydrogen atom moves 0.31 Å upward towards to basal plane of the carbon where the C–H bond distance d_H is about 1.10 Å, slightly smaller than that of graphene (1.12 Å) [60]. The atomic distortions are not negligible for the second and third neighbors of the hydrogen-bonded carbon atom (see Fig. S1 (b) of the Supplementary Material). Hence, the adsorbed hydrogen atom induces local lattice distortion. In previous studies [31,32,61], a single hydrogen atom prefers to bind to sp-hybridized carbon atoms in sp-sp^2 carbon network, and to sp^2-hybridized carbon atoms in sp^2-sp^3 carbon network. Likewise, for the H/TH-carbon, the hydrogen atom energetically favors adsorbing on sp^2-hybridized carbon atoms rather than sp^3-hybridized carbon atoms. Hybridization of the hydrogen-bonded carbon atom (C_1) changes from sp^2 into sp^3, breaking relevant π bonds. This is denoted as "sp^3-hydrogenation". The electronic and magnetic properties of H/TH-carbon (given in Fig. 2 (b) and (c) and Fig. S2 of the Supplementary Material) will be discussed in the following sections.

Considering the possible experimental realization of the proposed TH-carbon, we analyzed its formation energy. We calculated the formation energy E_f per C atom using the following equation $E_f = E_{2D} - E_{3D}$ where E_{2D} and E_{3D} are per C atom energies of 2D and the reference bulk materials, respectively. The low formation energy suggests the ease fabrication of 2D materials from their bulk counterparts. More specifically, the E_f ¡ 200 meV/C implies that the 2D materials can be synthesized as free standing such as graphene, BN, and MoS2 [1,62–64]. For the other 2D materials (graphdiyne [18], silicene [65], and ZnO [66]) which have been synthesized experimentally on the substrate, the E_f value is higher than 200 meV/C [67]. For instance, the E_f of 823 meV/C graphdiyne experimentally synthesized on the copper surface [18]. For TH-carbon, the E_f is found to be 920 meV/C, and hence it would be required a suitable substrate. On the other hand, hydrogenated TH-

Table 1
Calculated structure parameters of TH-carbon and its hydrogenated derivatives in 2×2 supercell. Here, the unitcell lattice constants a and b, buckling height h, bond lengths between two C_1 atoms d_{11}, and between C_1 and C_2 atoms d_{12}, between H and C_1 atom d_H in Å, and the bond angle between carbon atoms (C_1–C_2–C_1) θ in °, the binding energy E_b with PBE and van der Waals corrections using Grimme's DFT-D2 [58] and DFT-D3 [59] methods in eV/H, the total magnetic moment M in μ_B, the electronic band gap energy E_g in eV are presented for all the considered structures.

Structure	a	b	h	d_{11}	d_{12}	d_H	θ	E_b^{PBE}	E_b^{DFT-D2}	E_b^{DFT-D3}	M	E_g	Type
TH-carbon	4.533	6.107	0.58	1.34	1.54	–	135.5	–	–	–	0	2.63	direct
H/TH-carbon	4.528	6.105	0.63	1.48	1.60	1.10	115.8	2.45	2.52	2.50	1.0	–	metallic
d-$CH_{0.17}$	4.500	6.075	0.81	1.48	1.58	1.10	116.0	2.40	2.47	2.45	1.34	–	metallic
s-$CH_{0.17}$	4.506	6.092	0.70	1.54	1.59	1.10	116.7	3.28	3.35	3.33	0	2.72	indirect
s-$CH_{0.33}$	4.483	6.069	0.69	1.52	1.57	1.10	116.9	3.24	3.33	3.30	0	3.45	indirect
d-$CH_{0.67}$	4.412	6.084	0.80	1.54	1.56	1.10	122.1	3.13	3.22	3.19	0	3.87	direct

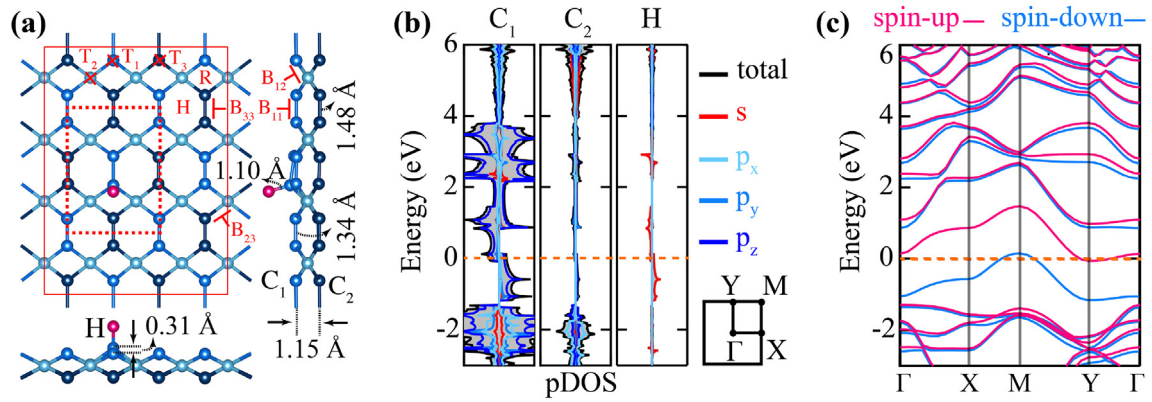

Fig. 2. (a) Atomic structure of the single hydrogen atom adsorbed on 2 × 2 TH-carbon supercell (denoted as H/TH-carbon). Top view from the *z* direction, side view from the *x* direction, and side view from the *y* direction are shown in the left upper panel, right upper panel, and lower panel, respectively. Here, all the considered adsorption positions (T_1, T_2, T_3, B_{11}, B_{12}, B_{23}, B_{33}, H, and R sites) are depicted. Carbon (C_1 and C_2) atoms and H atom are shown in blue colors and pink color, respectively. (b) Projected density-of-states (pDOS) of carbon (C_1 and C_2) and hydrogen (H) atoms in H/TH-carbon. (c) Electronic band structure with spin-up and spin-down states shown in pink and blue, respectively. Note that the Fermi level (E_F) is set to zero (depicted by the orange dashed line). (A colour version of this figure can be viewed online.)

carbon (d-$CH_{0.67}$) is more energetically favorable (16.8 eV lower energy than TH-carbon per unitcell). The possible experimental realization of the proposed hydrogenated TH-carbons, their fabrications from pristine TH-carbon would require the additional reaction of hydrogen atoms to the sp^2-hybridized carbon atoms. To estimate the initial step of this reaction, we first considered the single hydrogen atom diffusion pathway to form the energetically favorable hydrogenated configuration. For the sake of this, we investigated migration pathways and diffusion energy barriers for the H/TH-carbon by using NEB calculations. Three typical diffusion pathways (namely Path I, Path II, and Path III) were set by considering the favorable sites for the H atom on TH-carbon. The atomic arrangements of the IS, TS, FS, and the converged MEP for the H atom along the considered paths are indicated in Fig. 3 (a). Our NEB calculation results show that the energy barriers for the single H atom to diffuse on TH-carbon along the Path I, Path II, and Path III are 1.68, 3.30, and 3.32 eV, respectively, (Fig. 3 (b)). These results of high energy barriers indicate the low possibility of hydrogen migration from one energetic site (T_1) to another. From the energetic point of view (considering the binding energy and the diffusion energy barriers), therefore, it is evident that the single hydrogen atom strongly binds to an sp^2-hybridized carbon atom (C_1) on TH-carbon. We further considered a typical dissociative adsorption reaction pathway of the first H_2 molecule to form the energetically favorable paired hydrogenated configuration. The equilibrium atomic configurations of IS, TS, FS, and the converged MEP for the H_2 molecule are presented in Fig. 3(c). From the energy profile as indicated Fig. 3(d), we found that the dissociative addition of hydrogen needs to overcome energy barrier of 2.33 eV. The negative reaction energy (−0.08 eV) denotes an exothermic addition of the H_2 molecule on TH-carbon. Such high energy barriers imply that the dissociative adsorption of molecular hydrogen on TH-carbon is unexpected to occur. Therefore, we would suggest to use hydrogen plasma where atomic hydrogen of either radical or ionic form can be maintained. The chemically active hydrogen would result in sp^3-hydrogenation with any sp^2-hybridized carbon atoms of TH-carbon, similar to the graphane formation [3], or a catalytic pathway would be required as in the case of hydrogenated graphene [68].

Subsequent to having established the most stable configuration for the H/TH-carbon, we then studied two hydrogen atoms adsorption on TH-carbon unitcell where the concentration of hydrogen atoms, Θ is 17%. To identify the most favorable position of two hydrogen atoms on TH-carbon, all possible combinations of hydrogen positions were considered. For the double-sided hydrogenation case (Θ = 17%) (Fig. 4 (a)), two hydrogen atoms favor adsorbing two adjacent sp^2-hybridized carbon atoms on opposite sides of TH-carbon layers (denoted as d-$CH_{0.17}$). In this case, the binding energy of hydrogen is 2.40 eV/H, which is 0.05 eV/H smaller than that of H/TH-carbon. We note that when two adjacent sp^2-hybridized carbon atoms are hydrogenated on the opposite sides of TH-carbon layer, the induced local strain on C_2 carbon atom compensates each other (see Fig. S1 (c) of the Supplementary Material), reducing the total energy. Another possible configuration for two hydrogen atoms adsorption on the opposite side of TH-carbon unitcell becomes dynamically unstable, as the phonon dispersion exhibits negative frequency mode (Fig. S3 of the Supplementary Material).

For the single-sided hydrogenation case (Θ = 17%, Fig. 4 (b)), s-$CH_{0.17}$, two hydrogen atoms prefer to bound to two adjacent sp^2-hybridized carbon atoms with strong binding energy of 3.28 eV/H. The distance between hydrogen atoms for the s-$CH_{0.17}$ is found to be 2.25 Å which is similar to "*ortho*-dimer" hydrogen configuration on graphene [69]. The hydrogen adsorbed carbon atoms move simultaneously in the same direction. The atomic distortions are negligible for the second and third neighbors of the hydrogen-bonded carbon atoms (Fig. S1 (d) of the Supplementary Material). The length of C_1–C_1 bond becomes close to the standard value of sp^3 C–C bonds (1.54 Å) (see Table 1). We should note that extra stability is gained through pairing. Similarly, the *ortho*-dimer configurations on graphene lattice exhibit strong stability as compared to other configurations of two hydrogen atoms [70].

We next studied the highest hydrogen coverage level on the single-sided TH-carbon (Θ = 33%). In practice, this would be the case where TH-carbon on a substrate is fully hydrogenated. This configuration is referred to as s-$CH_{0.33}$ at which all the sp^2-hybridized carbon atoms on the single-sided of TH-carbon are hydrogenated (Fig. 4 (c)). The calculated binding energy is found to be 3.24 eV/H, which is 0.04 eV lower than that of s-$CH_{0.17}$. For the double-sided hydrogenation of TH-carbon with Θ = 33%, two possible hydrogenated derivatives, d^1-$CH_{0.33}$ and d^2-$CH_{0.33}$, were considered (Fig. S4 of the Supplementary Material). The binding energy for d^1-$CH_{0.33}$ and d^2-$CH_{0.33}$ are found to be 3.20 and 3.24 Å, respectively.

Last, we examined the highest hydrogen coverage level (Θ = 67%) where all the sp^2-hybridized carbon atoms are hydrogenated

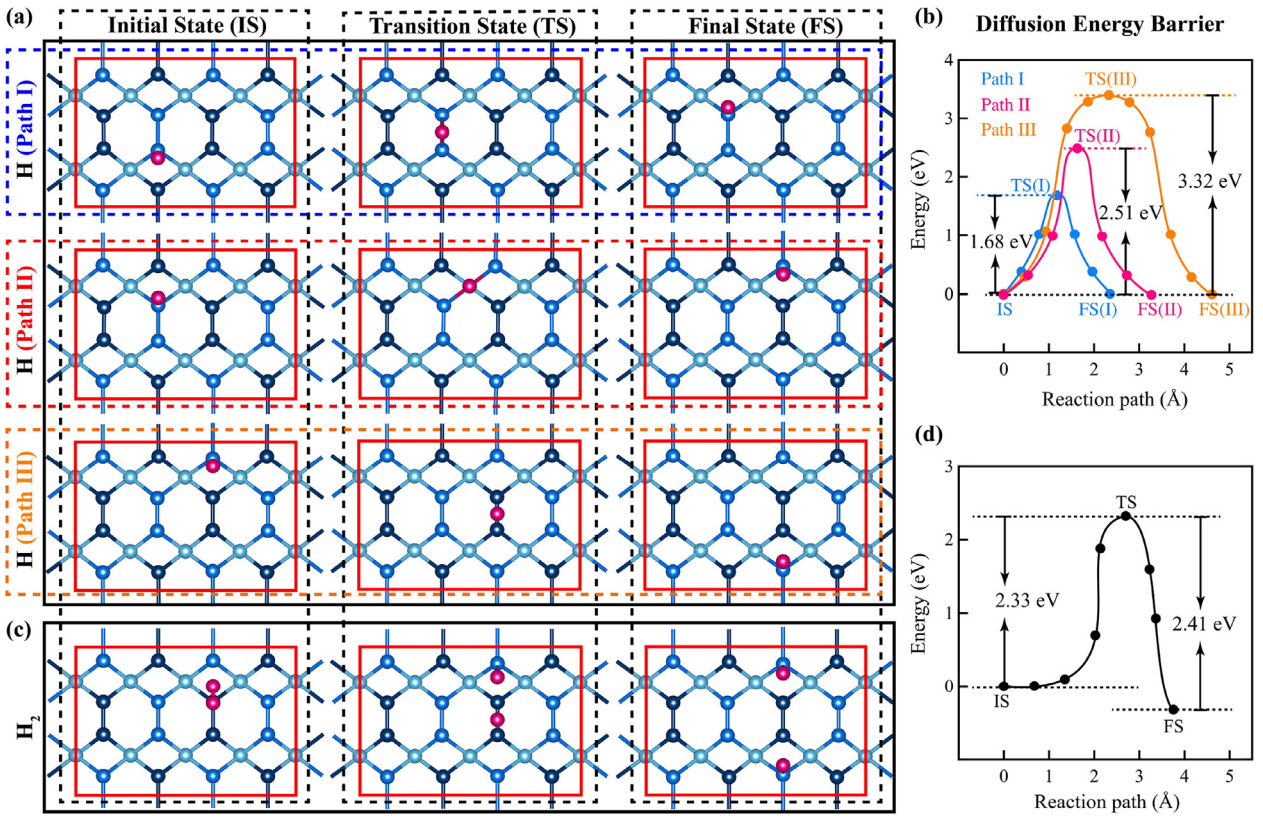

Fig. 3. (a) Energy pathways for a single H atom on TH-carbon along the different reaction pathways: namely Path I, Path II, and Path III. The equilibrium atomic configurations of the initial state (IS), transition state (TS), and final state (FS) for the each path are presented. Note that the IS and FS are energetically favorable adsorption sites for the single H atom adsorption on TH-carbon. (b) Diffusion energy barrier and minimum energy path (MEP) for the H atom along the Path I, Path II, and Path III. Here, the energy of the IS is set to 0 eV. (c) and (d) the equilibrium configurations for IS, TS, and FS and energy barrier of the dissociation of one H2 molecule adsorbed on TH-carbon, respectively. (A colour version of this figure can be viewed online.)

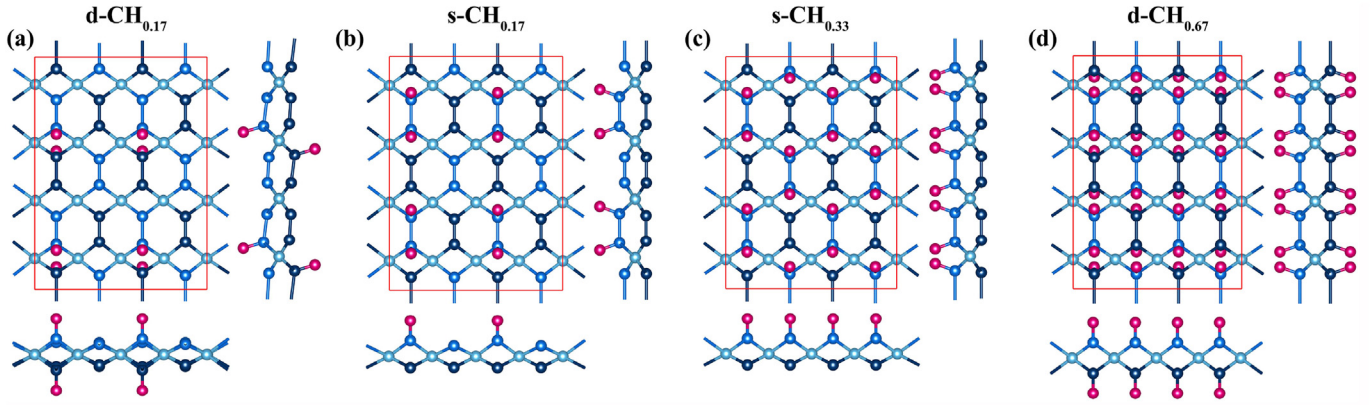

Fig. 4. Stable atomic configurations for single-sided and double-sided hydrogenation of TH-carbon (in 2 × 2 supercell) with different coverage levels. (a) d-$CH_{0.17}$, (b) s-$CH_{0.17}$, (c) s-$CH_{0.33}$, and (f) d-$CH_{0.67}$. Here, "s" and "d" denote the single- and double-sided hydrogenation, respectively, e.g., s-$CH_{0.33}$ represents the single-sided hydrogenation with $\Theta = 33\%$ coverage level. The blue and pink balls represent C and H atoms, respectively. (A colour version of this figure can be viewed online.)

on both sides of the TH-carbon sheet (Fig. 4 (d)). This configuration is referred to as d-$CH_{0.67}$. Upon full hydrogenation in TH-carbon, the structure becomes more symmetric in terms of the carbon-carbon bond lengths and bond angles as presented in Fig. S1 (e) of the Supplementary Material). For instance, the distance between sp^2-hybridized carbon atoms (d_{11}) increases from 1.34 to 1.54 Å with hydrogenation resulting in equal bond lengths, which is almost the same as that of diamond [71] or graphane (1.54 Å) [2]. Furthermore, the calculated binding energy is about 3.13 eV/ H, which is relatively lower than that of s-$CH_{0.33}$ by 0.11 eV/H. As mentioned above, for the case of double-sided hydrogenation, the induced local strain compensates each other, reducing the total energy. Regarding the maximum hydrogen capacity, the highest hydrogen concentration for hydrogenated TH-carbon is the same as that of fully hydrogenated-PG (C_3H_2) [72], but lower than graphane (CH) [3].

From the structural point of view, the transformation of the sp^2-hybridized carbon (C_1) in pristine TH-carbon to the sp^3

hybridization in hydrogenated TH-carbon results in a change in the buckling height h, and bond length (d_{11}) (see Table 1). As the hydrogen coverage increases, the h value gradually increases leading to considerable decrease in the lattice constants (a and b). Although the d_{11} slightly increases with the sp^3-hybridization, the relaxed lattice constants a and b decrease by about 2.7% and 1.0% respectively in comparison with those of pristine TH-carbon. We further studied the effect of the external strain on the lattice and adsorption properties since the materials are sensitive to the external conditions in various engineering applications [73]. A range of both compressive and tensile uniaxial strain along the lattice parameter **a** and **b** (referred to as uniaxial-x and uniaxial-y, respectively) and equi-biaxial strain from −2% to +10% with intervals of 2% were applied to the pristine TH-carbon, s-$CH_{0.33}$, and d-$CH_{0.67}$ systems. The variations of the h, d_{11}, and d_{12} with respect to the corresponding strain are presented in Fig. S5 of the Supplementary Material. Similar to PG [74], in the presence of the uniaxial-x, uniaxial-y, and equi-biaxial tensile strain, the h value decreases while the d_{11} and d_{12} values monotonically increase as the tensile strain increases. The results show the opposite behavior when subject to compressive strain. We note that the variations in the lattice parameters for the pristine TH-carbon and its hydrogenated derivatives are similar trends in the presence of the strain. Besides, we investigated the influence of mechanical deformation on the adsorption characteristics of a single H on TH-carbon. The preferred binding position of the single H on TH-carbon maintained in the corresponding strain ranges. As the pristine TH-carbon and its hydrogenated derivatives undergo compressive and tensile strains, it is observed that the binding energy gradually decreases, indicating less stable adsorption (see Fig. S6 of the Supplementary Material).

We should note that the hydrogen binding energy for hydrogenated TH-carbons was also calculated with the van der Waals (vdW) DFT-D2 and DFT-D3 correction methods of Grimme [58,59], which is important to test and modify the adsorption energy [75]. The calculated adsorption energies of hydrogenated TH-carbon with and without vdW corrections are summarized in Table 1, suggesting that the effect of vdW corrections on the adsorption energies of hydrogenated TH-carbon is subtle and negligible.

3.2.2. Dynamic stability and phonon properties

To examine the dynamic stability of TH-carbon and its hydrogenated derivatives, phonon frequencies of all modes are calculated as a function of the k-points in the BZ. The structure is identified to be stable if all the phonon modes are positive frequencies. The results from *ab-initio* lattice dynamics calculations are presented in Figs. 1 (b) and Fig. 5. We note that TH-carbon and its hydrogenated derivatives show positive frequencies for all modes in their BZ, and thus, they are dynamically stable.

Similar to graphene, three acoustic phonon branches such as transverse in-plane (TA), longitudinal (LA), and out-of-plane (ZA) for each considered systems were observed. The TA and LA branches exhibit linear features whereas the feature of ZA branch exhibits quadratic dispersion near Γ-point. We should note that the hydrogenated TH-carbon structures also have dispersionless C−H stretching modes at around 88 THz (see Fig. S4 (b) and (e)) [76]. Therefore, the hydrogenated TH-carbon has large bond-stretching phonon frequencies.

More interestingly, a remarkable phonon gap in the phonon spectra of pristine and partially hydrogenated TH-carbon sheets is observed (see the sky blue region in Fig. 5). The existence of the phononic gap can limit the contribution of phonon in thermal properties, which could be useful for thermoelectric devices. In order to interpret this gap in the phonon spectra, the atom-projected phonon density of states (PDOS) calculations were performed using the first-principles calculations. The phonon PDOS for pristine TH-carbon and its hydrogenated derivatives indicates that the phonon modes of sp^2-hybridized carbon atoms (C_1) are predominant in the high-frequency region (around 50 THz). Similar behavior was observed in the phonon modes of sp^2-sp^3 carbon networks such as in PG [22]. It is noted that the phonon branches at around 50 THz are gradually annihilated by increasing hydrogenation due to the sp^3-hydrogenation. Fig. 5 (d), the phonon spectra of fully hydrogenated TH-carbon (denoted as d-$CH_{0.67}$) composed of only sp^3 bonds, obviously shows the disappearance of corresponding phonon branches at high frequencies as well as the phonon gap. This result suggests that the phononic band gap of TH-carbon can be tuned by controlled hydrogenation.

3.2.3. Thermal stability and properties

We first focused on the thermal stability of TH-carbon and its hydrogenated derivatives. The thermal stability for the considered systems was investigated by *ab-initio* molecular dynamics (AIMD) simulations. To reduce the constraint of periodic boundary condition and explore possible structure reconstruction, we considered a 4 × 3 supercell and performed AIMD simulation with increasing temperature from 300 K to 900 K.

After energy minimization at 0 K, the systems were heated to 300 K to ensure thermal equilibrium for 1 ps. Thereafter, the TH-carbon systems (which are equilibrated at 300 K) were gradually heated to 900 K for 2.5 ps. Upon reaching a temperature of 900 K, the TH-carbon systems were thermally equilibrated for 2.5 ps. To ensure thermal equilibrium at 900 K, we monitored their potential energy with respect to time. The snapshots of atomic configurations for pristine TH-carbon and its hydrogenated derivatives at 900 K are shown in Fig. S7 of the Supplementary Material. It is

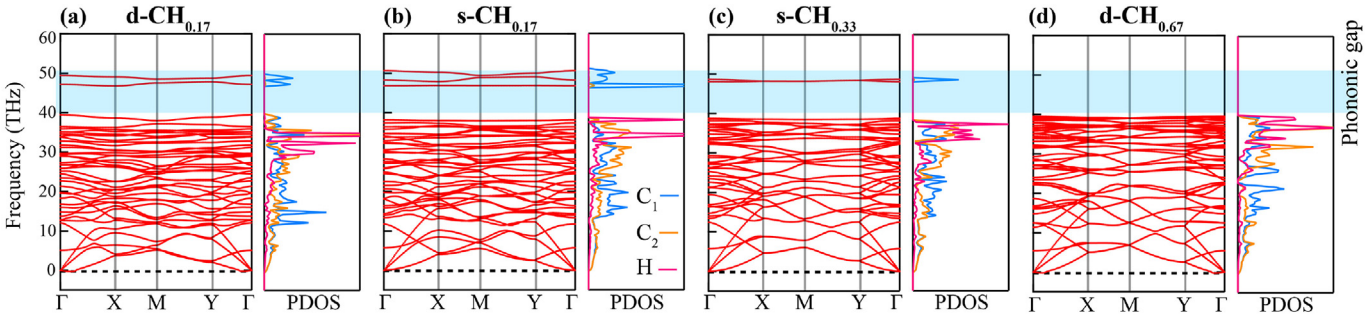

Fig. 5. Calculated phonon dispersion curves (left) and the atom-resolved phonon density of states (PDOS) (right) of hydrogenated derivatives of TH-carbon for (a) d-$CH_{0.17}$, (b) s-$CH_{0.17}$, (c) s-$CH_{0.33}$, and (d) d-$CH_{0.67}$. Here, the phononic gaps are marked with the shaded blue regions. Note that, the structures have totally positive phonon modes, indicating their dynamics stability. (A colour version of this figure can be viewed online.)

evident that the pristine TH-carbon and its hydrogenated derivatives preserve their planar configurations without any significant distortion even at 900 K. Even if the present simulation time is very short due to the computational limit in the AIMD calculations, this result at least shows that the structure is stable with respect to the thermal shock.

Next, we studied their thermal properties from the phonon calculations. 2D materials possess unusual phonon spectra due to the presence of out-of-plane modes, which makes them ideal candidates for thermal management applications [77]. Recent studies have examined the influence of hydrogenation on the thermal properties of carbon-based materials. For instance, hydrogenation of graphene leads to a dramatic decrease in thermal conductivity [78] while hydrogenation of PG leads to a large improvement in thermal conductivity [43]. With this motivation, we studied the thermal properties of pristine TH-carbon and its hydrogenated derivatives which are not reported yet. There are two main contributions to the thermal properties of the nanomaterials: the lattice vibrations (phonons) and electrons. The electron contribution is proportional to DOS at the Fermi level. Since most of the TH-carbon systems considered in the present work have a wide band gap (see in Fig. 8), their thermal properties would be dominated by the phonon contribution. We thus examined the thermal properties of pristine TH-carbon and its hydrogenated derivatives due to the lattice vibrations, which are responsible for the characteristic properties of the considered systems such as lattice thermal conductivity and specific heat.

By solving linearized phonon Boltzmann equation within the single-mode relaxation time approximation (RTA) [55], we calculated the lattice thermal conductivity (κ_L), which can be obtained from Eq. (2):

$$\kappa = \frac{1}{NV_0}\sum_{\lambda} C_\lambda \nu_\lambda \otimes \nu_\lambda \tau_\lambda \tag{2}$$

where N, V_0, λ are the total number of q points sampling in the BZ, the volume of a unitcell, and phonon mode, respectively, and C_λ, ν_λ, and τ_λ are the specific heat, phonon group velocity, and phonon lifetime, respectively. The C_λ is the mode dependent heat capacity, which can be obtained from Eq. (3):

$$C_V = \left(\frac{\partial E}{\partial T}\right)_V = C_\lambda = \sum_{\lambda} k_B \left(\frac{\hbar\omega_\lambda}{k_B T}\right)^2 \frac{exp\left(\frac{\hbar\omega_\lambda}{k_B T}\right)}{\left(exp\left(\frac{\hbar\omega_\lambda}{k_B T}\right) - 1\right)^2} \tag{3}$$

where k_B and $\hbar$ are the Boltzmann constant and reduced Planck constant, respectively.

Based on the second and third-order interatomic force constants obtained from the supercell method, we calculated the temperature-dependent lattice thermal conductivity of pristine and hydrogenated TH-carbon. Fig. 6 (a) shows that the κ_L decreases as the temperature increases due to the intrinsic enhancement of phonon-phonon scattering with temperature increasing. We found that the thermal transport in TH-carbon is anisotropic due to its inherent structural anisotropy. At room temperature, the calculated κ_L of pristine TH-carbon is about 419.15 and 342.30 W m^{-1} K^{-1} along with the **a** and **b** lattice directions, respectively, where the thickness of TH-carbon is taken as the interlayer equilibrium spacing of the sheet (2.75 Å [23]).

With increasing hydrogen coverage on TH-carbon, the structure has two domains, one with low conduction (sp^3 C–H bonds) and other with high thermal conduction (C–C bonds). For the single-sided full hydrogenation coverage (Θ = 33%), the κ_L of s-$CH_{0.33}$ is found to be 320.63 and 284.70 W m^{-1} K^{-1} along with the **a** and **b** lattice directions, respectively. The decreasing in thermal conductivity is attributed to the introduction of sp^3 C–H bonds in the structure. More specifically, a strong sp^2 C_1–C_1 bond (composed of σ and π bonds) gradually diminishes and deteriorates by hydrogenation, and becomes a weaker single σ bond (see Fig. 8, lower panels). Upon full hydrogen coverage (Θ = 67%), d-$CH_{0.67}$, the κ_L value significantly decreases to about 33.56 and 36.63 W m^{-1} K^{-1} along with the **a** and **b** lattice directions, respectively. This is attributed to the decreased phonon lifetime (Fig. S8 of the Supplementary Material). For graphene, the thermal conductivity decreases with increasing hydrogen coverage from 0% to 30%, and then insensitive to further H-coverage [78,79]. As a result, the heat transport in TH-carbon can be controlled by the sp^3 C–H low conduction domains.

We next showed the results on the lattice specific heat capacity at constant volume (C_v) for pristine TH-carbon and its hydrogenated derivatives in Fig. 6 (b). The specific heat capacity of pristine TH-carbon and its hydrogenated derivatives are almost identical at low temperature (below 300 K). However, the values become different at the higher temperature. The heat capacity of hydrogenated TH-carbon for d-$CH_{0.67}$ is found to be 29.4% larger than that for pristine TH-carbon at 1000 K. The reason for the higher specific heat capacity in hydrogenated TH-carbon is the existence of the high frequency C–H modes to gain extra vibrational energy. Similar behavior has been reported for graphane [80] and hydrogenated PG [72]. It is widely known that the sp^3-hydrogenation enhances the specific heat capacity. For instance, the heat capacity for graphane was reported to be 14.8% larger than that for graphene at 1000 K [81]. Furthermore, the phonon frequencies of sp^2-hybridized carbon atoms (C_1) at high frequency completely soften with hydrogenation, which increases the DOS at lower frequencies (see Figs. 1 (b) and Fig. 5). Therefore, the softening of acoustic and optical branches in the transverse direction results in the larger specific heat capacity by hydrogenation [80,82]. The large improvement in specific heat capacity would make hydrogenated TH-carbon suitable for storing and transferring energy.

3.2.4. Mechanical stability and properties

The mechanical stability of pristine TH-carbon and its hydrogenated derivatives was first tested by the following stability conditions (Born-Huang criteria [83]) of the elastic constants: $C_{11}\,C_{22} - C_{12}^2 > 0$ and $C_{66} > 0$. Here, C_{11}, C_{22}, C_{12}, and C_{66} are components of elastic modulus tensor. We calculated the corresponding elastic constants (C_{11}, C_{22}, C_{12}, and C_{66}) under the in-plane uniaxial, biaxial and shear strain conditions (see Fig. S9 of the Supplementary Material). The corresponding elastic constants can be derived from the second derivative of total energy with respect to the in-plane strain at equilibrium area by Eq. (4) and Eq. (5):

$$U(\varepsilon) = \frac{1}{2}C_{11}\varepsilon_{xx}^2 + \frac{1}{2}C_{22}\varepsilon_{yy}^2 + C_{12}\varepsilon_{xx}\varepsilon_{yy} + 2C_{66}\varepsilon_{xy}^2 \quad , \tag{4}$$

$$C_{ij} = \left(\frac{1}{S_0}\right)\left(\frac{\partial^2 U}{\partial \varepsilon^2}\right) \tag{5}$$

where U, C_{ij}, ε_{ij}, and S_0 are the elastic strain energy per unit area, in-plane stiffness, the infinitesimal strain tensors, and the equilibrium area, respectively. Here, the uniaxial strains along the **a** and **b** lattice directions (namely, uniaxial-x and uniaxial-y, respectively) are defined as $\varepsilon_x = (a\text{-}a_0)/a_0$ and $\varepsilon_y = (b\text{-}b_0)/b_0$, respectively, where a, b, and a_0, b_0 are the lattice constants of the strained and unstrained structures. We used the Voigt notation: i.e, $1 \rightarrow xx$, $2 \rightarrow yy$, and $6 \rightarrow xy$.

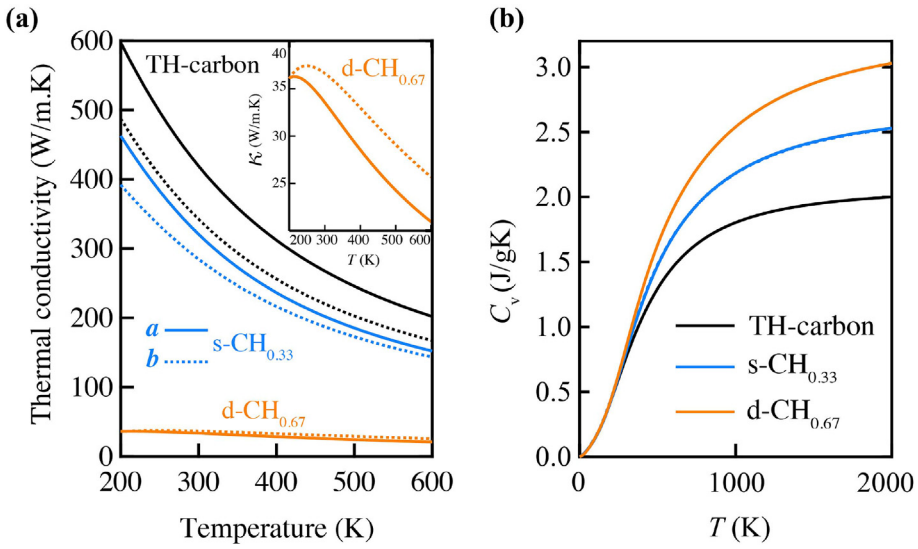

Fig. 6. (a) Lattice thermal conductivity (κ_L) and (b) specific heat capacity (C_V) at constant volume (V) for pristine TH-carbon, s-$CH_{0.33}$, and d-$CH_{0.67}$ as a function of T presented in black, blue, and orange, respectively. Here, the κ_L along with the **a** and **b** lattice directions are depicted by line and dashed lines, respectively. (A colour version of this figure can be viewed online.)

By changing the lattice constants of TH-carbon and its hydrogenated derivatives, a series of lateral strain in the range from −0.025 to 0.025 along the corresponding directions with an increment of 0.005 were applied to the TH-carbon sheets. At each point, the atomic positions were relaxed to calculate the total energies and the stress for each strain case. From strain-energy relationship (as presented in Fig. S9 of the Supplementary Material), we calculated the C_{ij} values as summarized in Table 2. Our calculated C_{11} and C_{22} values for pristine TH-carbon (287.03 N/m and 280.70 N/m, respectively) agree well with the report of Ram et al. [23]. We further reported C_{12} and C_{66} values for pristine TH-carbon, which are not reported yet. The calculated non-zero elastic constants in Table 2 meet the Born-Huang criteria of the mechanical stability ($C_{11} > |C_{12}|$ and $C_{66} > 0$) for all the considered TH-carbon sheets. Therefore, the TH-carbon and its hydrogenated derivatives are mechanically stable.

We next focus on their mechanical properties, in-plane Young's modulus Y, and Poisson's ratio P, which are calculated via the following equations:

$$Y = \frac{C_{11}^2 - C_{12}^2}{C_{11}}, \quad P = \frac{C_{12}}{C_{11}} \tag{6}$$

For the pristine TH-carbon, Young's moduli along the **a** and **b** lattice directions were calculated to be $Y_a = 286.12$ N/m and $Y_b = 279.88$ N/m, respectively, which are higher than that of PG (reported to be 263.8 N/m) [22]. As shown in Table 2, hydrogenation of TH-carbon reduces the Young's modulus. This reduction in Young's Modulus for the d-$CH_{0.67}$ is calculated to be 13% and 29% along the **a** and **b** directions with respect to the pristine TH-carbon, respectively. For hydrogenated PG and graphane, the reduction in Young's Modulus is also reported as 26% [84] and 30% [85] with respect to their pristine structures (PG and graphene), respectively. Likewise, shear modulus G also decreases with increasing hydrogen concentration. To understand the reduction of Young's modulus by hydrogenation, we turn to the nature of bonds and binding energy of the systems. It must be noted that the buckling height (h) increases with increasing hydrogen concentration, resulting in increased C_1–C_1 bond length (d_{11}), and the binding energy (E_b) slightly decreases with hydrogenation. The bond elongation and decreased E_b would result in the reduction of Young's modulus. Unlike PG, TH-carbon and its hydrogenated derivatives exhibit positive Poisson's ratio (P). The P_a and P_b tend to increase as the concentration of hydrogen in the TH-carbon system increases.

Table 2
Calculated elastic constants C_{ij} in N/m, Young's Modulus (Y) in N/m, and Poisson's Ratios (P) along **a** and **b** lattice directions of TH-carbon and its hydrogenated derivatives.

	C_{11}	C_{22}	C_{12}	$C_{66}(G)$	Y_a	Y_b	P_a	P_b
TH-carbon	287.03	280.82	16.21	123.99	286.12	279.88	0.06	0.06
d-$CH_{0.17}$	270.97	239.91	18.87	101.64	269.65	238.42	0.07	0.08
s-$CH_{0.17}$	279.24	258.34	18.74	112.44	277.98	256.98	0.07	0.07
s-$CH_{0.33}$	275.39	236.72	26.99	106.68	272.74	233.64	0.10	0.11
d-$CH_{0.67}$	252.92	204.31	32.03	82.222	248.87	199.29	0.13	0.16

We also calculated the ultimate strength of the pristine TH-carbon and its hydrogenated derivatives. To examine the ultimate strength, we plot the stress-strain curve for TH-carbon and its hydrogenated derivatives in Fig. 7. The stress-strain curve for PG is also presented as a benchmark for comparison. Our results show that the in-plane stress monotonically increases to reaches the maximum stress with increasing applied tensile strain. The calculated strain at the maximum strength for PG is 21% as in the previous report [22]. Those for pristine TH-carbon, s-$CH_{0.33}$, and d-$CH_{0.67}$ are 20, 21, and 25%, respectively.

3.2.5. Electronic properties

We will now report the electronic properties by analyzing the electronic band structure, the density of state (DOS), the charge distribution at valence band maximum (VBM) and conduction band minimum (CBM), and the electron localization function (ELF).

We start with the discussion of the electronic properties of the pristine TH-carbon (see Fig. 1 (c)). Based on the GGA scheme, its VBM and CBM are located at Gamma point, and its energy gap is about 1.62 eV when using PBE. Due to the underestimation of the band gap value with the PBE, we performed hybrid functional calculations for more accurate electronic band gaps using the HSE06. Its electronic band-gap energy is found to be 2.633 eV. The charge density of VBM and CBM is predominantly localized on sp^2-hybridized carbon atoms (C_1) atoms (Fig. 1 (d)). According to

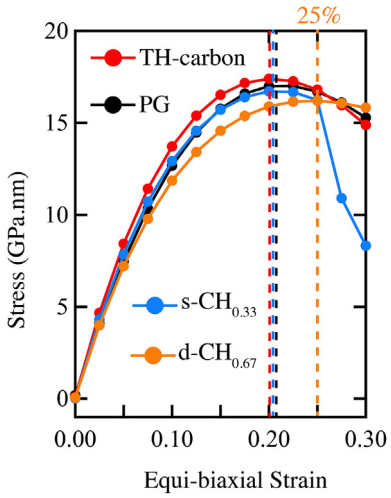

Fig. 7. Stress-strain relationship under applying equi-biaxial tensile strain for the PG, pristine TH-carbon, s-$CH_{0.33}$, and d-$CH_{0.67}$, represented in black, red, light blue and orange, respectively. Here, the maximal tensile stress points for each considered systems are depicted by dashed line. (A colour version of this figure can be viewed online.)

the atom/orbital projected density of states (pDOS) results (presented in Fig. S10 of the Supplementary Material), the electronic states near the Fermi energy level are mainly of p_z orbital of the C_1. All these results for pristine TH-carbon are in good agreement with the report of Ram et al. [23].

Next, we explain how hydrogen atoms affect the electronic and magnetic properties of the TH-carbon. According to the spin-polarized calculations, the spin projected density of states (DOS) indicates that the spins (up and down) are aligned near the Fermi energy level by means of exchange interactions. The obtained results show that the DOS of occupied state (below Fermi level) has the majority of spin-up electrons, which induces the spin polarization with the magnetic moment of about 1.0 μ_B (Fig. 2 (b)). The magnetic moment induced by the H atom adsorption is widely known for the other carbon allotropes (graphite [86], graphene [69,87], graphyne [88], and PG [72]). According to the pDOS of H/TH-carbon (Fig. S2 (b) of the Supplementary Material), the main contribution near the Fermi level originated from the p_z orbital of the nearest neighbor carbon (C_1) of the hydrogen-bonded carbon atom. This indicates that the adsorption of the H atom locally removes the p_z orbitals from the bonded sp^2-hybridized carbon atom (C_1), resulting in the electron localization and the change of the charge distribution (Fig. S2 (c) of the Supplementary Material). The electronic band structure for H/TH-carbon are presented in Fig. 2 (c). We observed that the adsorption of H atom leads to the disappearance of the band gap near the Fermi level for H/TH-carbon. Bader analysis of electron distribution [89] indicates that charge transfer occurs from H to C atoms upon hydrogen adsorption.

The electronic band structures of other hydrogenated TH-carbon sheets are presented in Fig. 8. The d-$CH_{0.17}$ is basically the same as the H/TH-carbon, where the broken bonds produce unpaired electrons with strong magnetic coupling between their spins. The hydrogen atoms in the d-$CH_{0.17}$ locally remove the corresponding p orbitals of the hydrogen-adsorbed carbon atoms in upper and lower planes as shown by the ELF profiles (Fig. 8 (a) lower panel). The electrons that were previously in the unhybridized p orbitals of the C_1 atoms in pristine TH-carbon are now localized at the C—H σ bond (the big red region in Fig. 8 (a) lower panel). We noted that the electron localization occurs around the center of all bonds, indicating the dominance of covalent bonding between pairs of atoms. It can be seen that the displacement of the hydrogen-bonded carbon atoms leads to an asymmetric bonding environment, which results in the distortion of the unhybridized p orbitals. According to the spin-polarized DOS, the spins (up and down) are aligned near the Fermi energy level by means of exchange interactions (see Fig. S10 (b) of the Supplementary Material). The total magnetic moment of the d-$CH_{0.17}$ is found to be 1.34 μ_B. Hydrogen induced magnetism in TH-carbon would be of great interest to spintronic device applications. The presence of electronic states at E_F indicates its metallic feature.

For the *ortho*-dimer hydrogen configurations, we studied the electronic properties of s-$CH_{0.17}$ and s-$CH_{0.33}$. The electronic band structure of the s-$CH_{0.17}$ exhibits an indirect gap with a magnitude

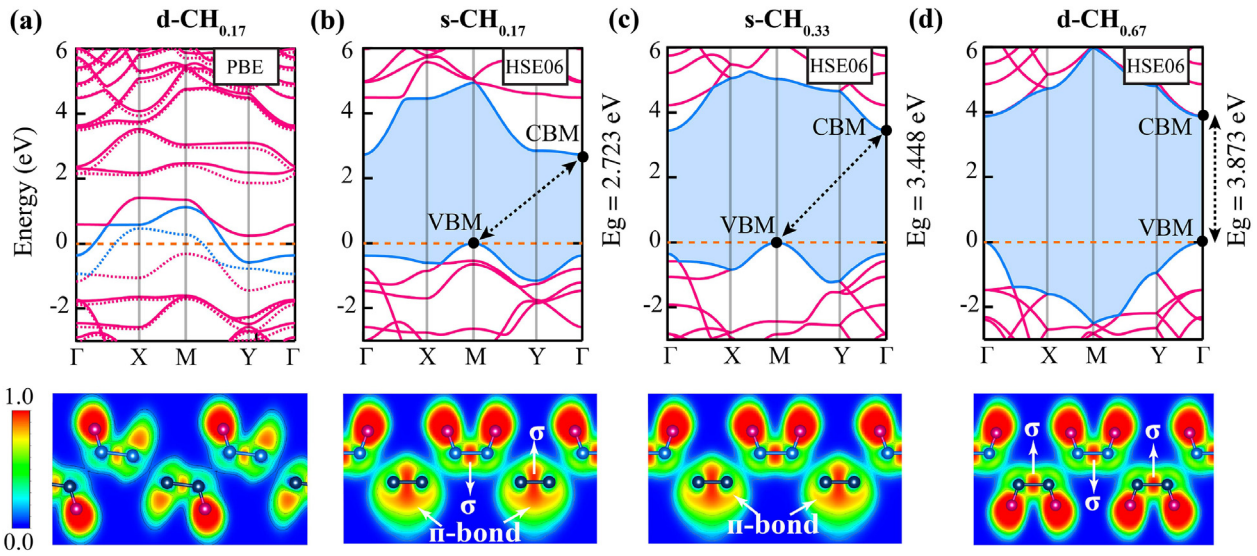

Fig. 8. Electronic band structure (upper panel) and electron localization function (ELF) plot (lower panel) for the hydrogenated derivatives of TH-carbon. (a) d-$CH_{0.17}$, (b) s-$CH_{0.17}$, (c) s-$CH_{0.33}$, and (d) d-$CH_{0.67}$. Here, direct and indirect bandwidths between valence band maximum (VBM) and conduction band minimum (CBM) are depicted with dashed black arrows. The Fermi level is shifted to 0 eV, and shown by the dashed orange line. The ELF profiles are depicted on the [100] plane. The ELF is dimensionless, and has a range from 0 to 1. ELF = 1 means highly localized and bounded electrons, while ELF = 0 means the lack of electron. (A colour version of this figure can be viewed online.)

of 2.723 eV (at which its VBM located to M point as presented in Fig. 8 (b)). The ELF profile is presented in Fig. 8 (b) (lower panel). We obtained that the nature of bonds (π and σ) between hydrogen-bonded carbon atoms (C_1–C_1) changed to pure σ bonding by hydrogenations, leading to the localized electron distribution. From the pDOS of the s-$CH_{0.17}$, the electronic states near the Fermi level disappear, which is expected as the contribution around the Fermi level comes mainly from the p_z orbitals of sp^2-hybridized C atoms. With increasing hydrogen coverage, the s-$CH_{0.33}$ exhibits the larger indirect band gap of 3.448 eV. This indicates that increasing the ratio of sp^3-hybridized carbon atoms leads to an increased band gap. It is worth noting that not only the ratio of sp^2- and sp^3-hybridized carbon atoms but also their spatial arrangements govern the electronic structure of TH-carbon (see Fig. S4 (c) and (f) of the Supplementary Material). The total magnetic moment for the *ortho* – dimer configuration is found to be zero. Upon pre-adsorbed H atom adsorption on TH-carbon, the second hydrogen atom vanishes the magnetization of the system. Similar behavior was reported in graphene that the *ortho*-dimer configurations to be nonmagnetic, while pre-adsorbed H atom to be magnetic [69,90].

For the highest coverage level ($\Theta = 67\%$), the electronic band structure of d-$CH_{0.67}$ turns to the wider direct band gap of 3.873 eV due to the rigid up-shift of the conduction band (Fig. 8 (d)). The wider direct band gap of the d-$CH_{0.67}$ would make it a good candidate for blue light-emitting diode (LED) applications. The band gap energy value of d-$CH_{0.67}$ is bigger than that for pristine TH-carbon but is smaller than that of purely sp^3-hybridized graphane (4.66 eV from DFT-GGA [41], 5.4 eV from accurate GW calculations [91]). In the d-$CH_{0.67}$ (fully hydrogenated TH-carbon), all the carbon atoms are sp^3-hybridized and electron bonds are saturated with hydrogen atoms, which result in insulating characteristics. The ELF profile of the d-$CH_{0.67}$ clearly showed that hydrogenation converts the orbitals of the sp^2-hybridized carbon atoms into sp^3, resulting in pure σ-bonding, and leading more symmetric and localized electron distribution (Fig. 8 (d) lower panel). We noted that the nature of bonds between sp^2 carbon atoms changes by hydrogenations. These results show that, upon changing the hydrogen coverage and configurations, the band gap of TH-carbon can be tuned in wide ranges (semiconductor and insulator), and also demonstrate the band gap transitions (direct to indirect semiconductor, metallic, and insulator).

To examine the optical properties of TH-carbon sheets would be beneficial to practical applications of the TH-carbon structures in optoelectronics since pristine TH-carbon and d-$CH_{0.67}$ exhibit the direct electronic band gap which plays an important role in the enhancement of the optical response of these materials. For the sake of this, we studied the optical properties of pristine TH-carbon, s-$CH_{0.33}$, and d-$CH_{0.67}$ such as the real($\varepsilon_1(\omega)$) and imaginary($\varepsilon_2(\omega)$) parts of dielectric function by applying the independent particle approximation as implemented in VASP [92]. The $\varepsilon_1(\omega)$ and $\varepsilon_2(\omega)$ as a function of photon energy for the TH-carbon systems depicted in Fig. 9. For the pristine TH-carbon, we observed the anisotropic optical behavior due to the inherent structural anisotropy in the sheet (i.e. all the sp^2-hybridized carbon atoms lie on the *b* lattice direction). This anisotropic feature could be utilized to determine the sample orientation experimentally by monitoring the absorption signal. As the hydrogenation structurally change the anisotropic of the TH-carbon to nearly isotropic, the anisotropic optical response virtually disappeared (see Fig. 9). Moreover, the absorption edge in the $\varepsilon_2(\omega)$ shifted to the higher energies by hydrogenation, which might improve the optical transparency. According to the a analysis of PDOS, the first absorption peaks of $\varepsilon_2(\omega)$ are mainly due to electron transition from 2*p* of C_1(valence band) to 2*p* of C_1(conduction band) (see Fig. S10 of the Supplementary Material).

We further studied the band gap variations as a function of strain and presented in Fig. S11 of the Supplementary Material. We observed that the pristine TH-carbon and its hydrogenated derivatives are sensitive to the external strain. However, the overall electronic structures are marginally affected by the strain, with only some changes in the bands energetic dispersion (see Fig. S12,

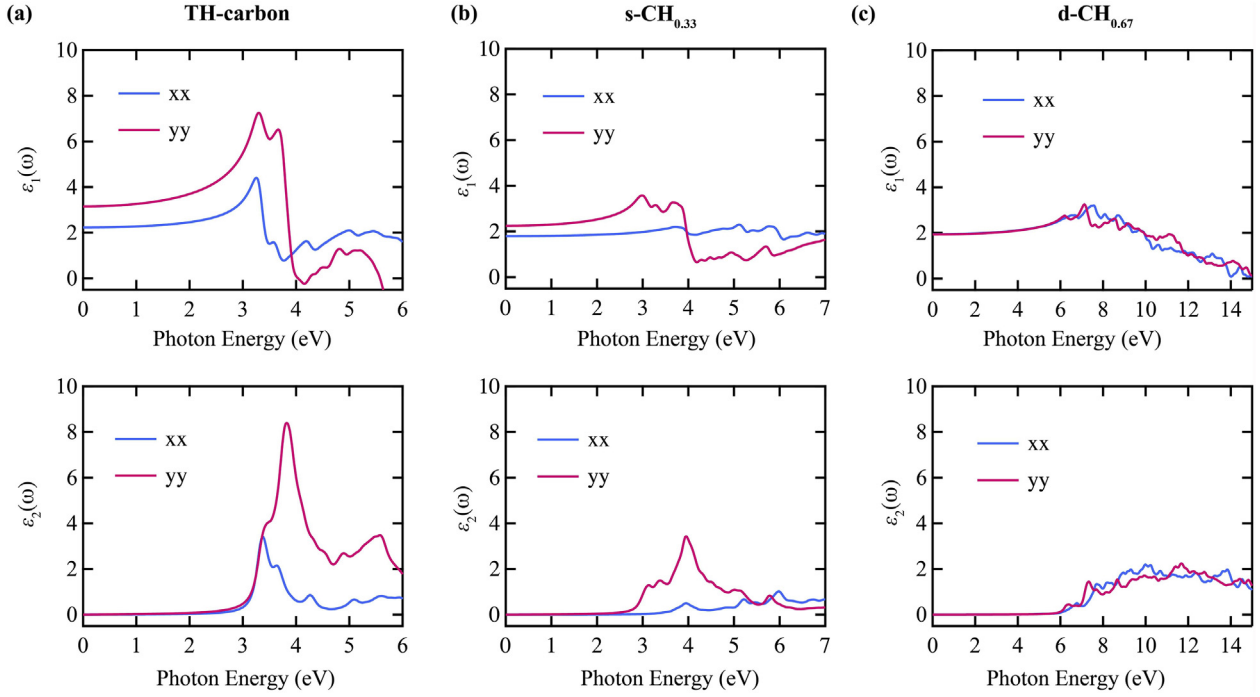

Fig. 9. The xx and yy component of real ($\varepsilon_1(\omega)$) and imaginary ($\varepsilon_2(\omega)$) parts of the dielectric function for (a) the pristine TH-carbon, (b) s-$CH_{0.33}$, and d-$CH_{0.67}$. (A colour version of this figure can be viewed online.)

Fig. S13, and Fig. S14 of the Supplementary Material). The band gap energy for the pristine TH-carbon decreases with increase in the uniaxial-*x* tensile strain, while it increases when compressive strains were applied. By contrast, in the presence of the uniaxial-*y* strain, the gap energy increases with increase tensile strain till 6.0% and then reduces with further strain, while it decreases under compressive strain. We note that all the sp^2-hybridized C_1-C_1 bonds lie on the **b** lattice directions, resulting in the different band gap behavior under strain. Therefore, due to the inherent structural anisotropy in the sheet, the band gap of TH-carbon systems exhibit anisotropic behavior.

4. Conclusions

The most significant result of the present work is to demonstrate the possibility of manipulating the physical and chemical properties of TH-carbon by hydrogenation, which affects the hybridization of the chemical bonds between carbon atoms. Our studies revealed their stabilities in the energetic, dynamic, thermal, and mechanical aspects. Depending on the hydrogen coverage and configurations, we observed the tunability of the phononic and electronic band gap, and the direct-indirect-direct band gap transitions, suggesting the plausibility of modulating the electronic properties of this novel carbon allotrope. The thermal transport in TH-carbon was found to be anisotropic. A significant decrease in thermal conductivity was observed by hydrogenation. The heat transport in TH-carbon can be controlled by the sp^3 C–H low conduction domains. Moreover, a notable increase in specific heat capacity was observed in hydrogenated derivatives of TH-carbon, which would make them useful in nanoscale engineering of thermal transport and heat management. Furthermore, the hydrogenation is found to reduce the in-plane stiffness and Young's modulus, but it increases the ultimate strength. The anisotropic optical behavior in TH-carbon due to the inherent structural anisotropy turns to nearly isotropic by hydrogenation. These findings provide important guidelines for the practical applications of TH-carbon and its hydrogenated derivatives in nanodevices and nanoelectronics.

Declaration of competing interest

The authors declare that they have no known competing financial interests or personal relationships that could have appeared to influence the work reported in this paper.

CRediT authorship contribution statement

Mehmet Emin Kilic: Conceptualization, Investigation, Writing - original draft, Writing - review & editing, Visualization. **Kwang-Ryeol Lee:** Supervision, Writing - review & editing.

Acknowledgements

We thank Dr. Hiroshi Mizuseki, Dr. Babu Ram, Dr. Deepika, Samuel Boateng, and Youngeun Na for fruitful discussions. We also gratefully acknowledge support by the Nano Materials Research Program through the Ministry of Science and IT Technology under Project NumberNRF-2016M3A7B4025402. The computing environment was prepared by Virtual Lab Inc.

Appendix A. Supplementary data

Supplementary data to this article can be found online at https://doi.org/10.1016/j.carbon.2020.01.027.

References

[1] K.S. Novoselov, A.K. Geim, S.V. Morozov, D. Jiang, Y. Zhang, S.V. Dubonos, I.V. Grigorieva, A.A. Firsov, Electric field effect in atomically thin carbon films, Science 306 (5696) (2004) 666–669.
[2] J.O. Sofo, A.S. Chaudhari, G.D. Barber, Graphane: a two-dimensional hydrocarbon, Phys. Rev. B 75 (15) (2007) 153401.
[3] D.C. Elias, R.R. Nair, T. Mohiuddin, S. Morozov, P. Blake, M. Halsall, A.C. Ferrari, D. Boukhvalov, M. Katsnelson, A. Geim, Control of graphene's properties by reversible hydrogenation: evidence for graphane, Science 323 (5914) (2009) 610–613.
[4] S.-H. Cheng, K. Zou, F. Okino, H.R. Gutierrez, A. Gupta, N. Shen, P. Eklund, J. Sofo, J. Zhu, Reversible fluorination of graphene: evidence of a two-dimensional wide bandgap semiconductor, Phys. Rev. B 81 (20) (2010) 205435.
[5] R. Baughman, H. Eckhardt, M. Kertesz, Structure-property predictions for new planar forms of carbon: layered phases containing sp 2 and sp atoms, J. Chem. Phys. 87 (11) (1987) 6687–6699.
[6] H. Okamoto, Y. Kumai, Y. Sugiyama, T. Mitsuoka, K. Nakanishi, T. Ohta, H. Nozaki, S. Yamaguchi, S. Shirai, H. Nakano, Silicon nanosheets and their self-assembled regular stacking structure, J. Am. Chem. Soc. 132 (8) (2010) 2710–2718.
[7] L. Song, L. Ci, H. Lu, P.B. Sorokin, C. Jin, J. Ni, A.G. Kvashnin, D.G. Kvashnin, J. Lou, B.I. Yakobson, Large scale growth and characterization of atomic hexagonal boron nitride layers, Nano Lett. 10 (8) (2010) 3209–3215.
[8] S.Z. Butler, S.M. Hollen, L. Cao, Y. Cui, J.A. Gupta, H.R. Gutiérrez, T.F. Heinz, S.S. Hong, J. Huang, A.F. Ismach, Progress, challenges, and opportunities in two-dimensional materials beyond graphene, ACS Nano 7 (4) (2013) 2898–2926.
[9] M. Dávila, L. Xian, S. Cahangirov, A. Rubio, G. Le Lay, Germanene: a novel two-dimensional germanium allotrope akin to graphene and silicene, New J. Phys. 16 (9) (2014), 095002.
[10] A.J. Mannix, X.-F. Zhou, B. Kiraly, J.D. Wood, D. Alducin, B.D. Myers, X. Liu, B.L. Fisher, U. Santiago, J.R. Guest, Synthesis of borophenes: anisotropic, two-dimensional boron polymorphs, Science 350 (6267) (2015) 1513–1516.
[11] S. Ipek, M. Kilic, A. Mogulkoc, S. Cahangirov, E. Durgun, Semiconducting defect-free polymorph of borophene: peierls distortion in two dimensions, Phys. Rev. B 98 (24) (2018) 241408.
[12] R. Pekoz, M. Konuk, M.E. Kilic, E. Durgun, Two-dimensional fluorinated boron sheets: mechanical, electronic, and thermal properties, ACS Omega 3 (2) (2018) 1815–1822.
[13] K.S. Novoselov, A.K. Geim, S. Morozov, D. Jiang, M.I. Katsnelson, I. Grigorieva, S. Dubonos, Firsov, Two-dimensional gas of massless Dirac fermions in graphene, Nature 438 (7065) (2005) 197.
[14] Y. Zhang, Y.-W. Tan, H.L. Stormer, P. Kim, Experimental observation of the quantum hall effect and berry's phase in graphene, Nature 438 (7065) (2005) 201.
[15] J.-A. Yan, W. Ruan, M. Chou, Phonon dispersions and vibrational properties of monolayer, bilayer, and trilayer graphene: density-functional perturbation theory, Phys. Rev. B 77 (12) (2008) 125401.
[16] R.B. Kaner, J.J. Gilman, S.H. Tolbert, Designing superhard materials, Science 308 (5726) (2005) 1268–1269.
[17] A. Hirsch, The era of carbon allotropes, Nat. Mater. 9 (11) (2010) 868.
[18] G. Li, Y. Li, H. Liu, Y. Guo, Y. Li, D. Zhu, Architecture of graphdiyne nanoscale films, ChemComm 46 (19) (2010) 3256–3258.
[19] B. Mortazavi, M. Makaremi, M. Shahrokhi, Z. Fan, T. Rabczuk, N-graphdiyne two-dimensional nanomaterials: semiconductors with low thermal conductivity and high stretchability, Carbon 137 (2018) 57–67.
[20] B. Mortazavi, M. Shahrokhi, T. Rabczuk, L.F.C. Pereira, Electronic, optical and thermal properties of highly stretchable 2d carbon ene-yne graphyne, Carbon 123 (2017) 344–353.
[21] B. Mortazavi, M. Shahrokhi, M.E. Madjet, M. Makaremi, S. Ahzi, T. Rabczuk, N-, p-, as-triphenylene-graphdiyne: strong and stable 2d semiconductors with outstanding capacities as anodes for li-ion batteries, Carbon 141 (2019) 291–303.
[22] Z. Shunhong, Z. Jian, W. Qian, C. Xiaoshuang, K. Yoshiyuki, J. Puru, Pentagraphene: a new carbon allotrope, Proc. Natl. Acad. Sci. U.S.A. 7 (2).
[23] B. Ram, H. Mizuseki, Tetrahexcarbon: a two-dimensional allotrope of carbon, Carbon 137 (2018) 266–273.
[24] L.-C. Xu, R.-Z. Wang, M.-S. Miao, X.-L. Wei, Y.-P. Chen, H. Yan, W.-M. Lau, L.-M. Liu, Y.-M. Ma, Two dimensional Dirac carbon allotropes from graphene, Nanoscale 6 (2) (2014) 1113–1118.
[25] D. Malko, C. Neiss, F. Vines, A. Görling, Competition for graphene: graphynes with direction-dependent Dirac cones, Phys. Rev. Lett. 108 (8) (2012), 086804.
[26] S. Kamalinahad, F. Viñes, P. Gamallo, Grazynes: carbon-based two-dimensional composites with anisotropic properties, J. Phys. Chem. C 123 (44) (2019) 27140–27149.
[27] N. Macmillan, The ideal strength of solids, in: Atomistics of Fracture, Springer, 1983, pp. 95–165.
[28] F.M. de Vasconcelos, A.G. Souza Filho, V. Meunier, E.C. Girão, Electronic properties of tetragraphene nanoribbons, Phys. Rev. Materials 3 (6) (2019), 066002.
[29] M.H. Sluiter, Y. Kawazoe, Cluster expansion method for adsorption: application to hydrogen chemisorption on graphene, Phys. Rev. B 68 (8) (2003),

085410.
[30] A. Savchenko, Transforming graphene, Science 323 (5914) (2009) 589–590.
[31] X. Li, S. Zhang, F.Q. Wang, Y. Guo, J. Liu, Q. Wang, Tuning the electronic and mechanical properties of penta-graphene via hydrogenation and fluorination, Phys. Chem. Chem. Phys. 18 (21) (2016) 14191–14197.
[32] J. Tan, X. He, M. Zhao, First-principles study of hydrogenated graphyne and its family: stable configurations and electronic structures, Diam. Relat. Mater. 29 (2012) 42–47.
[33] M. Pumera, C.H.A. Wong, Graphane and hydrogenated graphene, Chem. Soc. Rev. 42 (14) (2013) 5987–5995.
[34] P. Sessi, J.R. Guest, M. Bode, N.P. Guisinger, Patterning graphene at the nanometer scale via hydrogen desorption, Nano Lett. 9 (12) (2009) 4343–4347.
[35] H. González-Herrero, J.M. Gómez-Rodríguez, P. Mallet, M. Moaied, J.J. Palacios, C. Salgado, M.M. Ugeda, J.-Y. Veuillen, F. Yndurain, I. Brihuega, Atomic-scale control of graphene magnetism by using hydrogen atoms, Science 352 (6284) (2016) 437–441.
[36] M. Shahrokhi, C. Leonard, Tuning the band gap and optical spectra of silicon-doped graphene: many-body effects and excitonic states, J. Alloy. Comp. 693 (2017) 1185–1196.
[37] B. Mortazavi, M. Shahrokhi, M. Raeisi, X. Zhuang, L.F.C. Pereira, T. Rabczuk, Outstanding strength, optical characteristics and thermal conductivity of graphene-like bc3 and bc6n semiconductors, Carbon 149 (2019) 733–742.
[38] J. Zhou, Q. Wang, Q. Sun, X. Chen, Y. Kawazoe, P. Jena, Ferromagnetism in semihydrogenated graphene sheet, Nano Lett. 9 (11) (2009) 3867–3870.
[39] Z. Luo, T. Yu, K.-j. Kim, Z. Ni, Y. You, S. Lim, Z. Shen, S. Wang, J. Lin, Thickness-dependent reversible hydrogenation of graphene layers, ACS Nano 3 (7) (2009) 1781–1788.
[40] L. Li, R. Qin, H. Li, L. Yu, Q. Liu, G. Luo, Z. Gao, J. Lu, Functionalized graphene for high-performance two-dimensional spintronics devices, ACS Nano 5 (4) (2011) 2601–2610.
[41] H. Gao, L. Wang, J. Zhao, F. Ding, J. Lu, Band gap tuning of hydrogenated graphene: H coverage and configuration dependence, J. Phys. Chem. C 115 (8) (2011) 3236–3242.
[42] D. Yi, L. Yang, S. Xie, A. Saxena, Stability of hydrogenated graphene: a first-principles study, RSC Adv. 5 (26) (2015) 20617–20622.
[43] X. Wu, V. Varshney, J. Lee, T. Zhang, J.L. Wohlwend, A.K. Roy, T. Luo, Hydrogenation of penta-graphene leads to unexpected large improvement in thermal conductivity, Nano Lett. 16 (6) (2016) 3925–3935.
[44] G. Kresse, J. Hafner, Norm-conserving and ultrasoft pseudopotentials for first-row and transition elements, J. Phys. Condens. Matter 6 (40) (1994) 8245.
[45] P.E. Blöchl, Projector augmented-wave method, Phys. Rev. B 50 (24) (1994) 17953.
[46] G. Kresse, D. Joubert, From ultrasoft pseudopotentials to the projector augmented-wave method, Phys. Rev. B 59 (3) (1999) 1758.
[47] J.P. Perdew, K. Burke, M. Ernzerhof, Generalized gradient approximation made simple, Phys. Rev. Lett. 77 (18) (1996) 3865.
[48] H.J. Monkhorst, J.D. Pack, Special points for brillouin-zone integrations, Phys. Rev. B 13 (12) (1976) 5188.
[49] J. Heyd, G.E. Scuseria, M. Ernzerhof, Hybrid functionals based on a screened coulomb potential, J. Chem. Phys. 118 (18) (2003) 8207–8215.
[50] J. Paier, M. Marsman, K. Hummer, G. Kresse, I.C. Gerber, J.G. Ángyán, Screened hybrid density functionals applied to solids, J. Chem. Phys. 124 (15) (2006) 154709.
[51] S. Nosé, A unified formulation of the constant temperature molecular dynamics methods, J. Chem. Phys. 81 (1) (1984) 511–519.
[52] S. Nosé, A molecular dynamics method for simulations in the canonical ensemble, Mol. Phys. 52 (2) (1984) 255–268.
[53] W.G. Hoover, Canonical dynamics: equilibrium phase-space distributions, Phys. Rev. A 31 (3) (1985) 1695.
[54] L. Chaput, A. Togo, I. Tanaka, G. Hug, Phonon-phonon interactions in transition metals, Phys. Rev. B 84 (9) (2011), 094302.
[55] A. Togo, L. Chaput, I. Tanaka, Distributions of phonon lifetimes in brillouin zones, Phys. Rev. B 91 (9) (2015), 094306.
[56] G. Henkelman, B.P. Uberuaga, H. Jónsson, A climbing image nudged elastic band method for finding saddle points and minimum energy paths, J. Chem. Phys. 113 (22) (2000) 9901–9904.
[57] B. Silvi, A. Savin, Classification of chemical bonds based on topological analysis of electron localization functions, Nature 371 (6499) (1994) 683.
[58] S. Grimme, Semiempirical gga-type density functional constructed with a long-range dispersion correction, J. Comput. Chem. 27 (15) (2006) 1787–1799.
[59] S. Grimme, J. Antony, S. Ehrlich, H. Krieg, A consistent and accurate ab initio parametrization of density functional dispersion correction (dft-d) for the 94 elements h-pu, J. Chem. Phys. 132 (15) (2010) 154104.
[60] A. Ranjbar, M.S. Bahramy, M. Khazaei, H. Mizuseki, Y. Kawazoe, First-principles study of structural stability, magnetism, and hyperfine coupling in hydrogen clusters adsorbed on graphene, Phys. Rev. B 82 (16) (2010) 165446.
[61] H. Zhang, H. Pan, M. Zhang, Y. Luo, First-principles prediction of a new planar hydrocarbon material: half-hydrogenated 14, 14, 14-graphyne, Phys. Chem. Chem. Phys. 18 (34) (2016) 23954–23960.
[62] J.N. Coleman, M. Lotya, A. O'Neill, S.D. Bergin, P.J. King, U. Khan, K. Young, A. Gaucher, S. De, R.J. Smith, et al., Two-dimensional nanosheets produced by liquid exfoliation of layered materials, Science 331 (6017) (2011) 568–571.
[63] X. Chen, J.F. Dobson, C.L. Raston, Vortex fluidic exfoliation of graphite and boron nitride, ChemComm 48 (31) (2012) 3703–3705.
[64] M.A. Lukowski, A.S. Daniel, F. Meng, A. Forticaux, L. Li, S. Jin, Enhanced hydrogen evolution catalysis from chemically exfoliated metallic mos2 nanosheets, J. Am. Chem. Soc. 135 (28) (2013) 10274–10277.
[65] A. Kara, H. Enriquez, A.P. Seitsonen, L.L.Y. Voon, S. Vizzini, B. Aufray, H. Oughaddou, A review on silicene–new candidate for electronics, Surf. Sci. Rep. 67 (1) (2012) 1–18.
[66] C. Tusche, H. Meyerheim, J. Kirschner, Observation of depolarized zno (0001) monolayers: formation of unreconstructed planar sheets, Phys. Rev. Lett. 99 (2) (2007), 026102.
[67] A.K. Singh, K. Mathew, H.L. Zhuang, R.G. Hennig, Computational screening of 2d materials for photocatalysis, J. Phys. Chem. Lett. 6 (6) (2015) 1087–1098.
[68] F. Costanzo, P.L. Silvestrelli, F. Ancilotto, Physisorption, diffusion, and chemisorption pathways of h2 molecule on graphene and on (2, 2) carbon nanotube by first principles calculations, J. Chem. Theory Comput. 8 (4) (2012) 1288–1294.
[69] L. Xie, X. Wang, J. Lu, Z. Ni, Z. Luo, H. Mao, R. Wang, Y. Wang, H. Huang, D. Qi, Room temperature ferromagnetism in partially hydrogenated epitaxial graphene, Appl. Phys. Lett. 98 (19) (2011) 193113.
[70] Y. Ferro, D. Teillet-Billy, N. Rougeau, V. Sidis, S. Morisset, A. Allouche, Stability and magnetism of hydrogen dimers on graphene, Phys. Rev. B 78 (8) (2008), 085417.
[71] L.S. Bartell, On the length of the carbon-carbon single bond, J. Am. Chem. Soc. 81 (14) (1959) 3497–3498.
[72] H. Einollahzadeh, S.M. Fazeli, R.S. Dariani, Studying the electronic and phononic structure of penta-graphane, Sci. Technol. Adv. Mater. 17 (1) (2016) 610–617.
[73] M.E. Kilic, S. Erkoc, Structural properties of pristine and defected zno nanosheets under biaxial strain: molecular dynamics simulations, J. Nanosci. Nanotechnol. 16 (2) (2016) 1506–1516.
[74] M. Shahrokhi, Tuning the band gap and optical spectra of monolayer penta-graphene under in-plane biaxial strains, Optik 136 (2017) 205–214.
[75] D. Wang, Y. Bao, T. Wu, S. Gan, D. Han, L. Niu, First-principles study of the role of strain and hydrogenation on c3n, Carbon 134 (2018) 22–28.
[76] L. Kyhl, R. Balog, T. Angot, L. Hornekaer, R. Bisson, Hydrogenated graphene on ir (111): a high-resolution electron energy loss spectroscopy study of the vibrational spectrum, Phys. Rev. B 93 (11) (2016) 115403.
[77] H. Song, J. Liu, B. Liu, J. Wu, H.-M. Cheng, F. Kang, Two-dimensional materials for thermal management applications, Joule 2 (3) (2018) 442–463.
[78] S.-K. Chien, Y.-T. Yang, C.-K. Chen, Influence of hydrogen functionalization on thermal conductivity of graphene: nonequilibrium molecular dynamics simulations, Appl. Phys. Lett. 98 (3) (2011), 033107.
[79] Q.-X. Pei, Z.-D. Sha, Y.-W. Zhang, A theoretical analysis of the thermal conductivity of hydrogenated graphene, Carbon 49 (14) (2011) 4752–4759.
[80] H. Peelaers, A. Hernandez-Nieves, O. Leenaerts, B. Partoens, F. Peeters, Vibrational properties of graphene fluoride and graphane, Appl. Phys. Lett. 98 (5) (2011), 051914.
[81] M. Neek-Amal, F. Peeters, Lattice thermal properties of graphane: thermal contraction, roughness, and heat capacity, Phys. Rev. B 83 (23) (2011) 235437.
[82] S. Mann, P. Rani, R. Kumar, G.S. Dubey, V. Jindal, Thermodynamic properties of pure and doped (b, n) graphene, RSC Adv. 6 (15) (2016) 12158–12168.
[83] M. Born, K. Huang, Dynamical Theory of Crystal Lattices, 1954. Oxford.
[84] M.-Q. Le, Mechanical properties of penta-graphene, hydrogenated penta-graphene, and penta-cn2 sheets, Comput. Mater. Sci. 136 (2017) 181–190.
[85] Q. Pei, Y. Zhang, V. Shenoy, A molecular dynamics study of the mechanical properties of hydrogen functionalized graphene, Carbon 48 (3) (2010) 898–904.
[86] P. Lehtinen, A.S. Foster, Y. Ma, A. Krasheninnikov, R.M. Nieminen, Irradiation-induced magnetism in graphite: a density functional study, Phys. Rev. Lett. 93 (18) (2004) 187202.
[87] D. Soriano, F. Munoz-Rojas, J. Fernández-Rossier, J. Palacios, Hydrogenated graphene nanoribbons for spintronics, Phys. Rev. B 81 (16) (2010) 165409.
[88] J. Drogar, M. Roknabadi, M. Behdani, M. Modarresi, A. Kari, Hydrogen adsorption on the α-graphyne using ab initio calculations, Superlattice microst 75 (2014) 340–346.
[89] G. Henkelman, A. Arnaldsson, H. Jónsson, A fast and robust algorithm for bader decomposition of charge density, Comput. Mater. Sci. 36 (3) (2006) 354–360.
[90] O.V. Yazyev, L. Helm, Defect-induced magnetism in graphene, Phys. Rev. B 75 (12) (2007) 125408.
[91] S. Lebegue, M. Klintenberg, O. Eriksson, M. Katsnelson, Accurate electronic band gap of pure and functionalized graphane from gw calculations, Phys. Rev. B 79 (24) (2009) 245117.
[92] B. Adolph, V. Gavrilenko, K. Tenelsen, F. Bechstedt, R. Del Sole, Nonlocality and many-body effects in the optical properties of semiconductors, Phys. Rev. B 53 (15) (1996) 9797.